Journal of Physics D: Applied Physics

PAPER • **OPEN ACCESS**

Effective group dispersion of terahertz quantum-cascade lasers

To cite this article: Benjamin Röben *et al* 2021 *J. Phys. D: Appl. Phys.* **54** 025110

View the article online for updates and enhancements.

You may also like

- Research progress in terahertz quantum-cascade lasers and quantum-well photodetectors
  Zhi-Yong Tan, , Wen-Jian Wan et al.
- Broadly tunable single-mode mid-infrared quantum cascade lasers
  Bo Meng and Qi Jie Wang
- Novel InP- and GaSb-based light sources for the near to far infrared
  Sprengel Stephan, Demmerle Frederic and Amann Markus-Christian

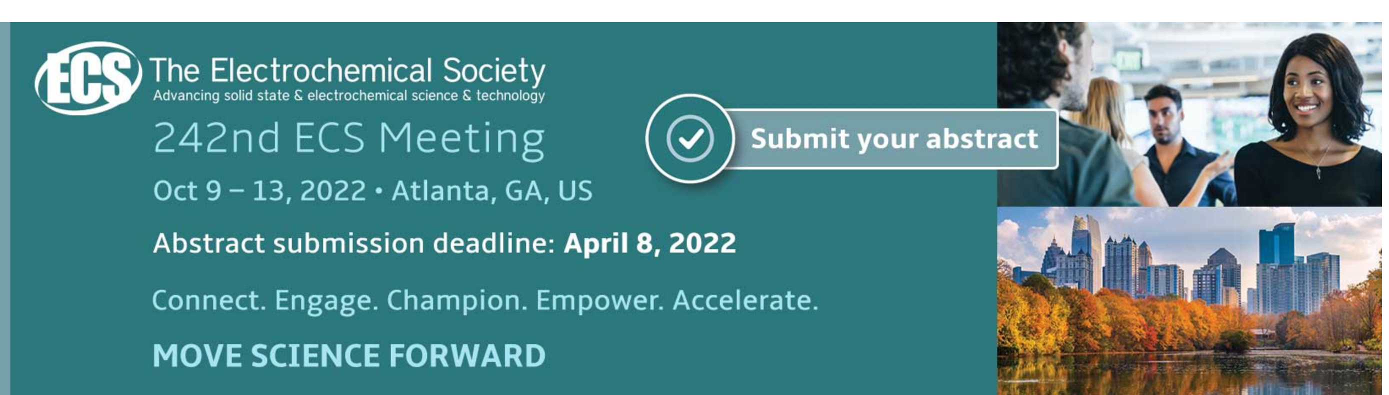

This content was downloaded from IP address 89.247.147.32 on 23/03/2022 at 06:52

OPEN ACCESS
IOP Publishing

Journal of Physics D: Applied Physics

J. Phys. D: Appl. Phys. **54** (2021) 025110 (10pp)

https://doi.org/10.1088/1361-6463/abbde3

Effective group dispersion of terahertz quantum-cascade lasers

Benjamin Röben, Xiang Lü, Klaus Biermann, Lutz Schrottke and Holger T Grahn

Paul-Drude-Institut für Festkörperelektronik, Leibniz-Institut im Forschungsverbund Berlin e.V., Hausvogteiplatz 5–7, 10117 Berlin, Germany

E-mail: roeben@pdi-berlin.de

Received 24 June 2020, revised 31 August 2020
Accepted for publication 2 October 2020
Published 22 October 2020

Abstract

Terahertz (THz) quantum-cascade lasers (QCLs) are based on complex semiconductor heterostructures, in which the optical gain is generated by intersubband transitions. Using the spacing of the laser modes in the emission spectra, we have determined the effective group refractive index $n_{g,\mathrm{eff}}$ for more than one hundred THz QCLs of the hybrid design with Fabry–Pérot resonators based on single-plasmon waveguides. The experimentally obtained values of $n_{g,\mathrm{eff}}$ for emission frequencies between 2.5 and 5.6 THz generally follow the trend of $n_{g,\mathrm{eff}}$ derived from electromagnetic simulations. However, for a certain number of QCLs, the experimental values of $n_{g,\mathrm{eff}}$ exhibit a rather large deviation from the general trend and the simulation results. From a thorough analysis, we conclude that differences in the optical gain/loss spectra are responsible for this deviation, which lead to a modification of the dispersion in the active region and consequently to altered values of $n_{g,\mathrm{eff}}$. The analysis also provides evidence that these differences in the gain/loss spectra originate from both, the details of the design and the gain broadening due to interface roughness.

Keywords: terahertz quantum-cascade lasers, group refractive index, Fabry–Pérot resonators, plasmon waveguides, GaAs/AlAs

(Some figures may appear in colour only in the online journal)

1. Introduction

Chromatic dispersion—often expressed in terms of the refractive index—determines the phase and group velocity of electromagnetic radiation as a function of its optical frequency. Since dispersion is a fundamental property of matter, it governs well-known optical phenomena such as refraction and reflection. In modern optics, dispersion is important for optical waveguides, since it determines effects such as pulse broadening and chirping. In waveguide lasers, dispersion influences the spectral emission parameters such as the mode spacing.

One of the most recent developments among waveguide lasers is the terahertz (THz) quantum-cascade laser (QCL) [1]. It is based on a cascaded semiconductor heterostructure within a single-plasmon [1, 2] or metal-metal [3] waveguide. THz QCLs are very attractive for spectroscopy, since they are compact and exhibit output powers of several mW as well as very narrow linewidths in the MHz to kHz range. In addition, they can be operated as frequency combs [4, 5], enabling the powerful dual-comb spectroscopic technique [6, 7]. A drawback is currently the operating temperature of THz QCLs, which lies below 130 K in continuous-wave [8] and 210 K in pulsed mode [9]. Fortunately, compact mechanical cryocoolers [10] allow for operation of optimized THz QCLs [11] without liquid cryogens, enabling practical

Original Content from this work may be used under the terms of the Creative Commons Attribution 4.0 licence. Any further distribution of this work must maintain attribution to the author(s) and the title of the work, journal citation and DOI.

 © 2020 The Author(s). Published by IOP Publishing Ltd Printed in the UK

applications despite their rather low operating temperatures. Recently, continuous-wave operation of a high-performance THz QCL has been demonstrated in an ultra-miniature cryocooler [12], further reducing the requirements for electrical power.

Just as for other waveguide lasers, the dispersion of THz QCLs is an important fundamental parameter. In transparent materials, the phase and group refractive indices determine the speed of the wavefronts and wavepackets, respectively. In waveguides, the presence of areas with different refractive indices results in waveguide modes whose propagation is described by an *effective* phase (n_{eff}) and group ($n_{g,\mathrm{eff}}$) refractive index.

So far, the literature on the dispersion of THz QCLs focuses on broadband active regions and metal-metal waveguides [13–15]. In contrast, we focus in this work on more narrowband active regions (bandwidths of typically 100 GHz) and single-plasmon waveguides. Narrowband active regions are favorable for the spectroscopy of particular atomic or molecular species due to the large spectral brightness of the QCLs. For such applications, THz QCLs with single-plasmon waveguides have the advantage of a rather directional emission [16]. In addition, these QCLs have shown to be reliable in many proof-of-principle spectroscopic experiments [17–21].

For the determination of the dispersion of semiconductor lasers operating in the visible to mid-infrared spectral region, the sub-threshold emission spectrum can be used [22, 23]. However, this approach is difficult to realize for THz QCLs due to the very low emission intensity below threshold. Alternatively, the dispersion can be derived from the analysis of short pulses transmitted through the lasers [24, 25]. For THz QCLs, this method is implemented by using THz time-domain spectroscopy, which employs the phase-sensitive detection of broadband THz pulses for the determination of $n_{g,\mathrm{eff}}$ [14, 15]. A second method, which we employ in this work, relies on the mode spacing in the emission spectrum of THz QCLs with Fabry–Pérot resonators [13, 26].

In this work, we investigate $n_{g,\mathrm{eff}}$ for a rather large number of different THz QCLs with emission frequencies between 2.5 and 5.6 THz using the emission spectra of QCLs based on active regions with both, $\mathrm{Al}_x\mathrm{Ga}_{1-x}\mathrm{As}$ ($x \leq 0.25$) and AlAs barriers. While the values of $n_{g,\mathrm{eff}}$ for QCLs with different emission frequencies largely follow a general trend, there are also some clear exceptions. We will discuss in detail the effect of different structural parameters such as the doping density as well as the influence of the intersubband transitions in the active region on $n_{g,\mathrm{eff}}$.

2. Group refractive index based on emission spectra

2.1. Experimental determination

Our approach to determine $n_{g,\mathrm{eff}}$ is based on the analysis of the emission spectra of THz QCLs with Fabry–Pérot resonators. The data base is provided by the emission spectra recorded during the standard characterization of our QCLs over the last ten years. The active regions of the QCLs have thicknesses of typically 11 μm and were grown using molecular beam epitaxy on semi-insulating GaAs substrates with diameters of 2 inches. After growth, single-plasmon waveguides with widths of 200 μm are processed. From the processed wafers, laser stripes are obtained by cleavage, which are soldered using indium to gold-plated copper submounts and wire-bonded for electrical contact. The waveguide mode in single-plasmon waveguides is confined at the top by the metallic contact layer. At the bottom, a 700 nm-thick Si-doped ($[\mathrm{Si}] = 2 \times 10^{18}$ cm^{-3}) layer is inserted as the lower contact. Since this layer provides only a limited confinement, the waveguide mode penetrates significantly into the substrate, which is semi-insulating to avoid free-carrier losses [2].

For the measurements of the emission spectra, the QCLs were operated at 10 K in pulsed mode typically at a repetition rate of 5 kHz with pulse widths of 500 ns, resulting in a duty cycle of 0.25%. All investigated QCLs have Fabry–Pérot resonators with lengths between 2.8 and 3.6 mm. The spectra were acquired with a Bruker IFS66v or a Bruker Vertex 80v Fourier transform infrared spectrometer at their highest resolutions of 3.6 or 2.1 GHz, respectively.

As an example, figure 1(a) shows the measured spectra at a resolution of 3.6 GHz for three different injection currents of a QCL with a design similar to the GaAs/AlAs QCL in reference [27]. The vertical, dotted lines in figure 1(a) mark the frequencies of the Fabry–Pérot modes for an injection current of 1.7 A, which exhibit a regular spacing as expected for the employed Fabry–Pérot resonator with a length of about 3 mm. Note that the widths of the peaks are determined by the instrument resolution. Figure 1(b) shows a plot of the peak frequencies based on the spectra recorded for 8 different injection currents for the same QCL as in figure 1(a). As the injection current is increased from 1.0 to 2.0 A, we observe mainly an increasing number of modes due to the higher gain at the edges of the gain profile. From 2.0 A onward, the emission range experiences a red shift due to the quantum-confined Stark effect. A frequency shift due to self-heating is negligible because of the pulsed operation with a low duty cycle. Over the entire current range, the individual modes experience a tuning toward lower frequencies, while the mode spacing remains constant. This red shift is indicated by the dashed lines in figures 1(a) and (b). A detailed analysis of the emission spectra confirms that—within the accuracy of the measurements—there is no dependence of the mode spacing on the injection current.

The effective group refractive index can be calculated based on the resonator length L and the frequency spacing $\Delta\nu$ between two adjacent Fabry–Pérot modes according to [28]

$$n_{g,\mathrm{eff}} = \frac{c}{2L\Delta\nu}\,, \tag{1}$$

where c denotes the speed of light. Hence, a value for $n_{g,\mathrm{eff}}$ can be calculated for every mode pair (adjacent modes) within every spectrum and different injection currents. Due to the limited accuracy of the measurements, there is a significant scattering of the different values of $n_{g,\mathrm{eff}}$ for a single QCL. We

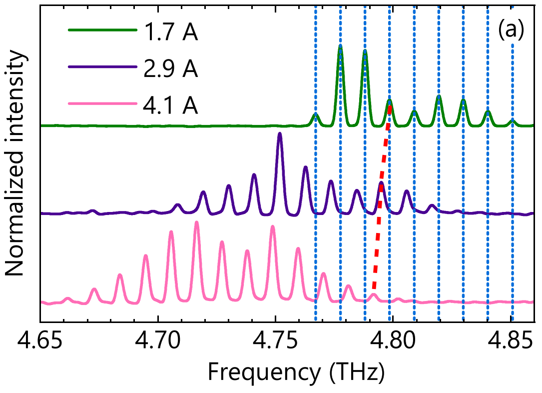

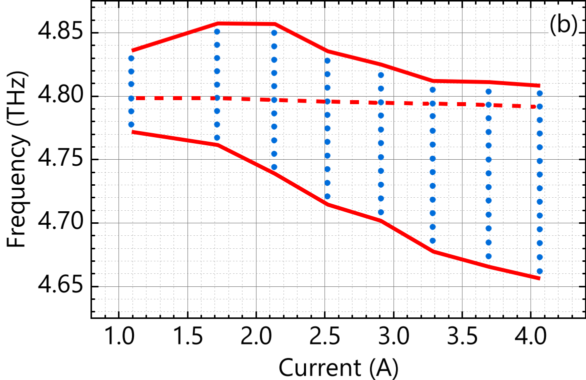

Figure 1. (a) Emission spectra measured for injection currents of 1.7, 2.9, and 4.1 A (top to bottom) of a QCL with a similar design as the GaAs/AlAs QCL in [27]. The vertical, dotted lines mark the frequencies of the peaks for an injection current of 1.7 A. The dashed line indicates the frequency tuning of a single mode. Note that the widths of the peaks are determined by the instrument resolution.
(b) Frequencies of the peaks (dots) in the spectra recorded for eight different injection currents for the same QCL as in (a). The solid lines represent the envelope of the modes, and the dashed line indicates the frequency tuning of a single mode.

therefore calculate for each QCL the mean and its standard deviation of the values for $n_{g,\mathrm{eff}}$ obtained within every spectrum for all investigated injection currents. This averaging procedure leads to a value of $n_{g,\mathrm{eff}}$ with a precision substantially higher than the one expected from the resolving power of the spectrometer, which is a measure for the precision of the frequencies of a *single* mode pair. The value of the mean of $n_{g,\mathrm{eff}}$ is assigned to the mean of the frequencies ν of all considered modes.

We validated that $n_{g,\mathrm{eff}}$ is independent from the injection current by determining $n_{g,\mathrm{eff}}$ as a function of the injection current for a QCL emitting at 4 THz. The required statistics for every value of $n_{g,\mathrm{eff}}$ was obtained by 4 repeated acquisitions of the spectrum for every investigated value of the injection current.

For the retrieval of the frequencies of the peaks in the spectra, we employed a peak finding algorithm with the parameters threshold, minimum sharpness, and Gaussian blurring. For every single spectrum, the peak finding parameters were adjusted in order to obtain an optimal result for the peaks found by the algorithm.

2.2. Assessment of measurement precision

In order to rule out relevant systematic errors related to the limited spectral resolution, we recorded high-resolution spectra with a resolution of 0.3 GHz for a number of different QCLs using a Bruker IFS120 HR Fourier transform spectrometer or the upgraded version IFS120/125 HR. Figure 2 shows a comparison of the values for $n_{g,\mathrm{eff}}$ based on low- and high-resolution measurements. The ellipses group the measurements for the same QCL. We observe that the values of $n_{g,\mathrm{eff}}$ for the low- and high-resolution measurements fully agree within the error margins and conclude that systematic errors due to the limited accuracy of the low-resolution measurements are negligible compared to the stochastic error. For the QCLs with frequencies above 3.45 THz as shown in figure 2, there is some deviation in the values of the frequency between the low- and high-resolution measurements.

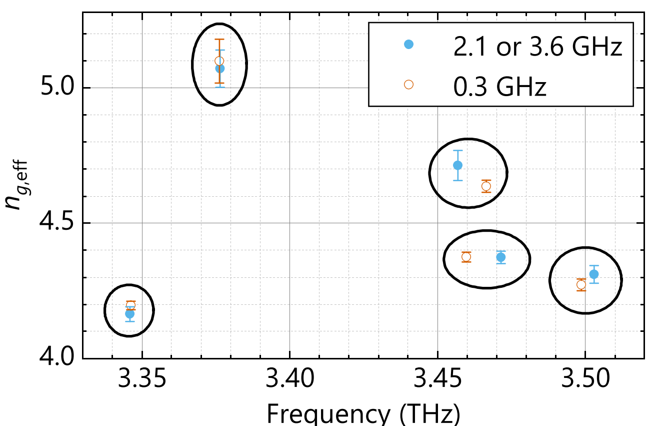

Figure 2. Values of $n_{g,\mathrm{eff}}$ of a number of different QCLs with AlAs barriers measured with low (2.1 or 3.6 GHz) and high (0.3 GHz) resolution. The ellipses group the results for the same QCL.

This small deviation arises because the number of the spectra and the investigated values of the injection current differ to some extent between the low- and high-resolution measurements. The maximum difference is on the order of 10 GHz, which is much smaller than the typical bandwidth of 100 GHz of our QCLs and is therefore negligible.

The measurement of the resonator length L is a further possible origin of errors, since $n_{g,\mathrm{eff}}$ also depends on L according to equation (1). The estimated absolute error of the length measurement using our optical microscope amounts to about $\pm 20\ \mu$m, which results in a relative error of $\pm 0.7\%$ based on the typical value for L of 3 mm. It is therefore smaller than the typical error of the measurement for the mode spacing amounting to $> \pm 1\%$.

2.3. Main results

Figure 3(a) shows the effective group refractive index $n_{g,\mathrm{eff}}$ of 121 different QCLs based on more than 800 spectra in total. Every dot represents one of the 79 QCLs with $Al_xGa_{1-x}As$

barriers ($x \leq 0.25$) and every circle one of the 42 QCLs with AlAs barriers. The investigated QCLs are all based on one particular design, the hybrid design described in [29], which is closely related to the designs described in [30, 31], but differs in the number of quantum wells. More details on the design and its modifications will be given in subsection 3.2. Most values of $n_{g,\mathrm{eff}}$ follow a general trend corresponding to an increase of $n_{g,\mathrm{eff}}$ with increasing emission frequency. This general trend is well described by the average function $\bar{n}_{g,\mathrm{eff}}(\nu)$ obtained by fitting all data points for $n_{g,\mathrm{eff}}$ in figure 3(a) excluding the values for the GaAs/AlAs QCLs below 4.5 THz, since these values clearly represent a rather large deviation from the general trend. The function $\bar{n}_{g,\mathrm{eff}}(\nu)$ is given by

$$\bar{n}_{g,\mathrm{eff}}(\nu) = A\mathrm{e}^{b\nu} + c \tag{2}$$

with $A = 0.0327$, $b = 0.717/\mathrm{THz}$, and $c = 3.566$. Here, ν denotes the frequency in THz. The obtained average function $\bar{n}_{g,\mathrm{eff}}(\nu)$ is shown as the dashed line in figure 3(a).

Figure 3(a) also shows the result for $n_{g,\mathrm{eff}}$ based on electromagnetic simulations (solid line), which underestimates the experimentally determined general trend to some extent. The simulations have been performed using the finite-element solver *JCMsuite* (JCMwave) based on frequency-dependent material permittivities (i.e. including material dispersion) [32, 33].

A possible reason for the deviation between $\bar{n}_{g,\mathrm{eff}}$ and the simulated $n_{g,\mathrm{eff}}$ as shown in figure 3(a) is an unreliable data set for the material dispersion, since there is rather little literature on low-temperature values of the dispersion of the (Al,Ga)As system in the THz frequency range. The deviation may also be related to the cavity pulling effect (also known as frequency pulling) [34]. The onset of the optical gain in a laser leads to a modification of the refractive index and hence to a difference between the frequency of the laser mode and the resonator mode without pumping and lasing. In contrast to the case of most other lasers, frequency pulling in THz QCLs can substantially contribute to the dynamic tuning induced by the injection current [35]. The influence of the gain on the refractive index is further discussed in subsection 3.3.

From the function $\bar{n}_{g,\mathrm{eff}}$, a function $\bar{n}_{\mathrm{eff}}$ for the phase refractive index can be retrieved using the relation [28]:

$$\bar{n}_{g,\mathrm{eff}} = \bar{n}_{\mathrm{eff}} + \nu \frac{\partial \bar{n}_{\mathrm{eff}}}{\partial \nu}\,. \tag{3}$$

We employ the exponential function

$$\bar{n}_{\mathrm{eff}}(\nu) = \tilde{A}\mathrm{e}^{\tilde{b}\nu} + \tilde{c} \tag{4}$$

as the ansatz for $\bar{n}_{\mathrm{eff}}(\nu)$ in equation (3). The free parameters of $\bar{n}_{\mathrm{eff}}(\nu)$ can then be numerically determined from equation (3) based on a fitting procedure of discretized values of $\bar{n}_{g,\mathrm{eff}}(\nu)$. This procedure yields the values $\tilde{A} = 0.0154$, $\tilde{b} = 0.589/\mathrm{THz}$, and $\tilde{c} = 3.60$ for the free parameters of $\bar{n}_{\mathrm{eff}}(\nu)$ according to equation (4). The validity of this procedure is verified by substituting the retrieved function $\bar{n}_{\mathrm{eff}}(\nu)$ based on these parameters into equation (3). The resulting function for $\bar{n}_{g,\mathrm{eff}}$ agrees with the dashed line in figure 3(a) so that the above retrieval procedure is self-consistent.

The retrieved function $\bar{n}_{\mathrm{eff}}(\nu)$ is shown in figure 3(b) (dashed line) along with a curve for n_{eff} (solid) obtained from electromagnetic simulations based on a finite-element solver. The function $\bar{n}_{\mathrm{eff}}(\nu)$ is offset to some extent with respect to the simulated curve, and its slope is somewhat steeper at higher frequencies.

Figure 3(b) also shows the material refractive index n_{GaAs} of GaAs at 5 K [32]. This function is employed in the simulation for the substrate and active region. We neglect the Al content in the active region amounting to about 3% due to a lack of suitable data in the literature around the operating temperature of 10 K. The values for n_{eff} are larger than the values for the material refractive index n_{GaAs} due to waveguide dispersion.

In order to investigate the differences in performance of different QCLs fabricated from the same wafer, figure 4 shows different groups of QCLs, where every QCL of a group is fabricated from the same wafer. Results of QCLs of a particular group are indicated by the same symbol in figure 4. Most of the values of $n_{g,\mathrm{eff}}$ for QCLs within every group agree very well within the error range, while the values for QCLs from wafers W1 and W2 as indicated in figure 4 exhibit a significant deviation in terms of $n_{g,\mathrm{eff}}$ and in part in terms of the emission frequency. The QCL of wafer W1 with the lower value for $n_{g,\mathrm{eff}}$ was fabricated from material located only 1.5 mm away from the wafer edge, while the distance from the wafer edge for the other QCL of wafer W1 amounts to more than 4 mm. Consequently, we attribute the difference in $n_{g,\mathrm{eff}}$ between the QCLs of wafer W1 to an altered layer sequence close to the wafer edge due to a radial inhomogeneity of the epitaxy process. This inhomogeneity appears to be particularly strong close to the wafer edge, since all other QCLs are fabricated from material at distances from the wafer edge of at least 4 mm.

The results of the QCLs from wafer W2 show a very large spread in the emission frequency. This behavior is attributed to the exceptionally large thickness of the active region of about 20 μm while the active regions of all other QCLs have thicknesses between 10 and 12 μm. The QCLs from W2 show a blue shift of the emission frequency toward the edge of the wafer. Despite the large spread in emission frequencies, the values of $n_{g,\mathrm{eff}}$ as a function of frequency follow the general trend $\bar{n}_{g,\mathrm{eff}}$ again rather well.

All results presented so far are based on spectra taken at about 10 K. We also checked the values of $n_{g,\mathrm{eff}}$ for operating temperatures up to 85 K based on a number of QCLs with both barrier types between 3.4 and 4.7 THz. We found a very good agreement within the confidence interval with the results of the measurements at 10 K (not shown). This behavior is expected, since the temperature-dependent tuning range is of similar magnitude as the tuning by means of the injection current.

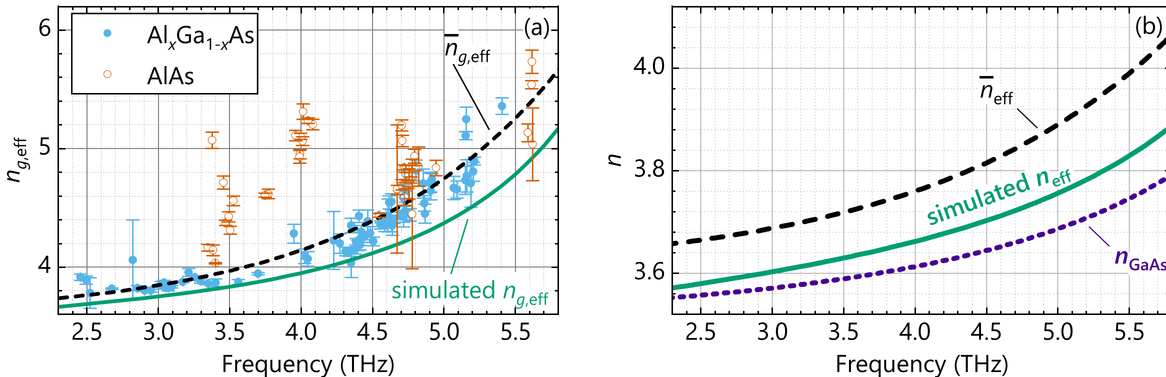

Figure 3. (a) Effective group refractive index $n_{g,\mathrm{eff}}$ of different THz QCLs with $\mathrm{Al}_x\mathrm{Ga}_{1-x}\mathrm{As}$ (dots) and AlAs (circles) barriers. The vertical error bars signify twice the standard deviation of the mean. The dashed line represents an average function $\bar{n}_{g,\mathrm{eff}}(\nu)$ of the measured values for $n_{g,\mathrm{eff}}$, which was obtained using a fit of all data excluding the values for QCLs with AlAs barriers below 4.5 THz, since they clearly represent a rather large deviation from the general trend. The solid line corresponds to a simulated curve for $n_{g,\mathrm{eff}}$. (b) Average effective phase refractive index $\bar{n}_{\mathrm{eff}}(\nu)$ (dashed line) derived from $\bar{n}_{g,\mathrm{eff}}(\nu)$ as shown in (a), simulated n_{eff} (solid line), and material refractive index n_{GaAs} of GaAs (dotted line).

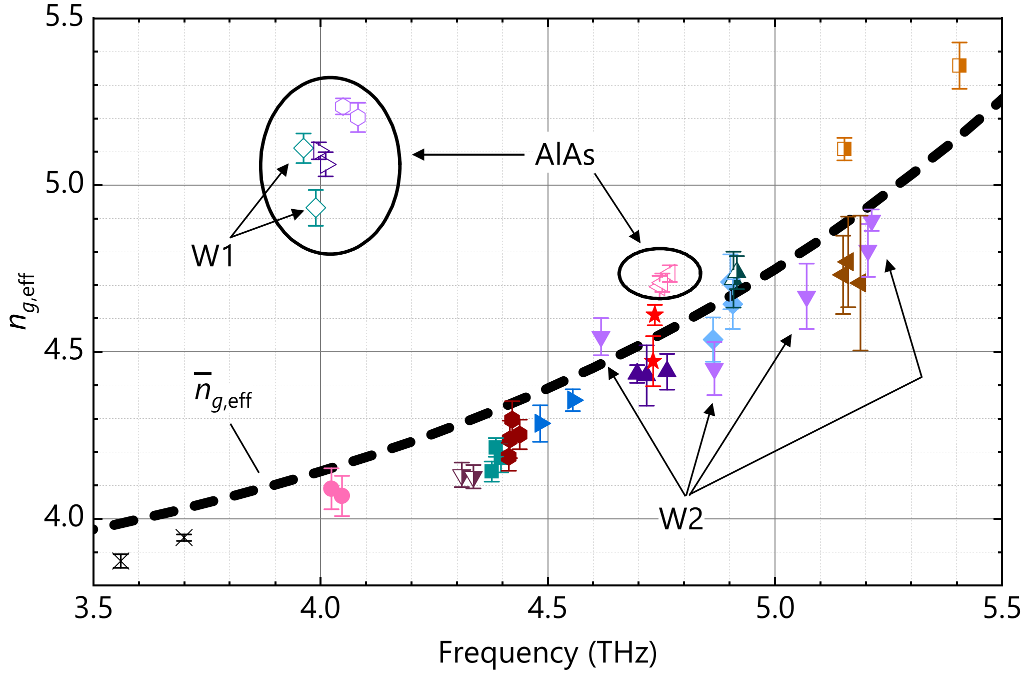

Figure 4. Comparison of the values for $n_{g,\mathrm{eff}}$ of QCLs with $\mathrm{Al}_x\mathrm{Ga}_{1-x}\mathrm{As}$ and AlAs barriers fabricated from 17 different wafers. QCLs made from the same wafer are marked by the same symbol. The data points marked by open symbols and additionally encircled by ellipses represent the results for QCLs with AlAs barriers, while the other data points are based on QCLs with $\mathrm{Al}_x\mathrm{Ga}_{1-x}\mathrm{As}$ barriers. The QCLs marked by W1 exhibit a comparatively large difference in $n_{g,\mathrm{eff}}$. Likewise, also QCLs from wafer W2 show significant deviations, which are discussed in the text.

3. Origin of the deviation from the general trend

In this section, several possible causes for the deviation from the general trend will be discussed. We will investigate the dependence of $n_{g,\mathrm{eff}}$ on the Al content, on the thickness of the active region, on the active-region design including the layer sequence and the doping density, and on the performance characteristics such as maximum output power, threshold current, or emission bandwidth. Finally, we will discuss the role of intersubband transitions as the main mechanism leading to changes in $n_{g,\mathrm{eff}}$.

3.1. Al content and thickness of active region

The fact that more than half of the QCLs with AlAs barriers follow the general trend quite well clearly shows that the

barrier type alone cannot be responsible for the large deviation from the general trend. In particular, the average Al content in the active regions with AlAs barriers is similar to the one in active regions with $Al_xGa_{1-x}As$ barriers, since the smaller thicknesses of the AlAs barriers compensate for the higher Al content within the barrier (i.e. for $x = 1$) with respect to $Al_xGa_{1-x}As$ barriers. Additionally, the variation in the average Al content, which ranges between 3 and 5.5% for $Al_xGa_{1-x}As$ barriers (smaller range for AlAs barriers), leads only to a marginal change in the refractive index according to calculations and is therefore not responsible for the differences in $n_{g,\mathrm{eff}}$.

The average Al content varies due to the different modifications of the basic design described in subsection 3.2. Figure 5(a) shows the deviation $\Delta n_{g,\mathrm{eff}}$ from the general trend $\bar{n}_{g,\mathrm{eff}}$ as a function of the average Al content of the active region for QCLs with emission frequencies smaller than 4.5 THz. This frequency range contains the QCLs with large deviations from $\bar{n}_{g,\mathrm{eff}}$ as well as some QCLs with a good agreement with $\bar{n}_{g,\mathrm{eff}}$. The results displayed in figure 5(a) clearly show that there is no dependence of $\Delta n_{g,\mathrm{eff}}$ on the average Al content. Calculations of the refractive index also show a negligible influence of the differences in Al content on the refractive index. In addition to the Al content changed on purpose due to a modification of the design, there might be an unintentional variation due to growth. However, the variation in the average Al content from 3.4% to 3.9% as displayed in figure 5(a) corresponds to a relative change in the Al content of more than 10%, which is much higher than what can be expected from an unintentional variation during growth. We therefore conclude that modifications in the average Al content due to design or unintentional variations are not responsible for the deviations from the general trend. Instead, there appears to be the tendency that $\Delta n_{g,\mathrm{eff}}$ depends on the specific design modification. In figure 5(a), QCLs with two slightly different nominal layer sequences denoted D4 and D5 are marked. The average Al contents of D4 and D5 are almost equal, since only a single layer for the entire QCL structure has been modified. The QCLs of these different design modifications have non-intersecting ranges of values for $\Delta n_{g,\mathrm{eff}}$. The different QCLs of each design modification exhibit either different doping densities or represent regrown samples. The dependence of $n_{g,\mathrm{eff}}$ on the nominal layer sequence and on the doping density will be discussed in detail in subsection 3.2.

Apart from the variations of the Al content of different QCLs, there are also some differences in the thicknesses of the active regions, while the widths of all investigated QCLs are identical, and the different lengths are accounted for in the calculation of $n_{g,\mathrm{eff}}$. Figure 5(b) shows $\Delta n_{g,\mathrm{eff}}$ as a function of the thickness of the active region for the GaAs/AlAs QCLs. We also added the values for $\nu > 4.5$ THz for completeness. There is no dependence of $\Delta n_{g,\mathrm{eff}}$ on the thickness of the active region, which agrees with the earlier result that the QCLs from wafer W2 follow the general trend quite well, although the thickness of the active region amounts to about 20 μm (cf figure 4).

3.2. Active-region design, growth conditions, and performance characteristics

The investigated QCLs are all based on the hybrid design consisting of alternating photon and longitudinal optical phonon-assisted transitions between quasi-minibands. The doping of the active region is usually restricted to one quantum well of the injector region. The doping may also play the role of creating a local dipole in front of the upper laser level, modifying the carrier transport in a non-linear way.

The designs of all investigated lasers originate from the design reported in reference [29] for a $GaAs/Al_{0.15}Ga_{0.85}As$ QCL. Design variations are mainly obtained by modifying the barrier height using $GaAs/Al_{0.18}Ga_{0.82}As$ [36], $GaAs/Al_{0.25}Ga_{0.75}As$ [37], and GaAs/AlAs [27] heterostructures and/or by scaling the layer structures to different emission frequencies [11, 38]. The design modifications have been carried out in such a way that the subband structure remains as similar as possible to the initial design. This similarity is exemplarily shown in figure 1 of reference [27] and in figure 1 of reference [11]. Further minor design modifications carried out for a small number of QCLs include injector regions with one quantum well removed or added, a modified width of the quasi-miniband, and small changes to individual layer thicknesses. The lasers with these minor design modifications follow the general trend $\bar{n}_{g,\mathrm{eff}}$ quite well except for design modification D3 shown in figure 6. Furthermore, four lasers emitting at around 3.0 THz, which are based on a hybrid design with shorter injector regions and shorter quasi-minibands for carrier extraction [39], also follow the general trend well.

In order to investigate the influence of the design modifications of the layer sequence and the nominal doping density on $n_{g,\mathrm{eff}}$, we focus on groups of QCLs with identical nominal layer sequences, but different nominal doping levels. Figure 6 shows the deviation $\Delta n_{g,\mathrm{eff}}$ from the general trend $\bar{n}_{g,\mathrm{eff}}$ as a function of the nominal doping density. Same symbols indicate the results for identical nominal layer sequences. The investigated design modifications of the layer sequence are referred to as D1 to D6. The design modifications D1 to D3 aimed at an emission frequency of 4.7 THz with D1 referring to the GaAs/AlAs QCL given in [27] and D2 to QCL B in [40], while D3 is a modification of D2 insofar as the injector region consists of 3 quantum wells with two of them doped. Based on these designs, D4 and D5 have been obtained mainly by scaling the layer structure to emission frequencies of 3.5 THz (QCL A in [11]) and D6 by a scaling to 3.9 THz (QCL B in [11]). The layer sequences for D4 and D5 are almost identical, since only one single layer for the entire QCL structure has been modified. In addition, the wafers for both groups of lasers have been grown and processed in different campaigns. Consequently, the two groups may also slightly differ with respect to the contact properties and to the ratio of the nominal to actual doping density.

In essence, figure 6 shows that differences in $\Delta n_{g,\mathrm{eff}}$ mainly depend on the particular design modification, while the nominal doping density has a rather small influence on $\Delta n_{g,\mathrm{eff}}$. As described in more detail in the following subsection 3.3,

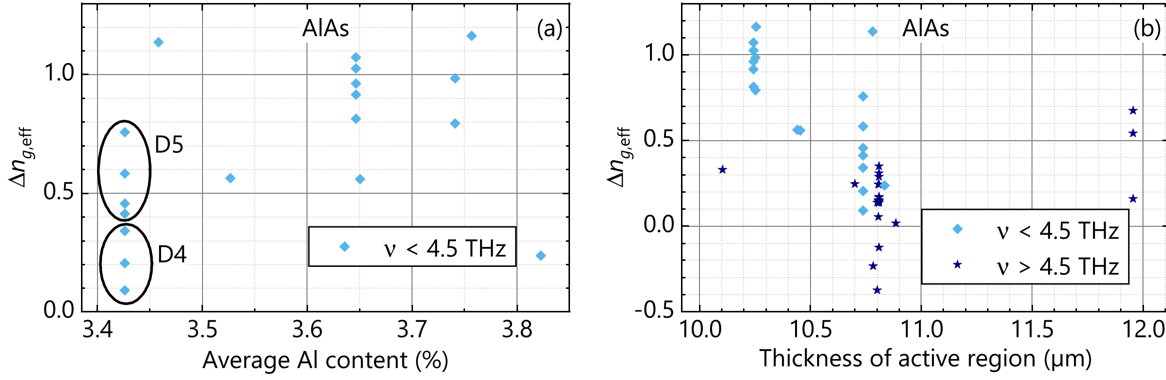

Figure 5. (a) Deviation $\Delta n_{g,\text{eff}} = n_{g,\text{eff}} - \bar{n}_{g,\text{eff}}$ from the general trend as a function of the average Al content of the active region for different QCLs with AlAs barriers and emission frequencies $\nu < 4.5$ THz. (b) Values for $\Delta n_{g,\text{eff}}$ as a function of the thickness of the active region for the same QCLs as in (a). For completeness, we also show the values for $\nu > 4.5$ THz.

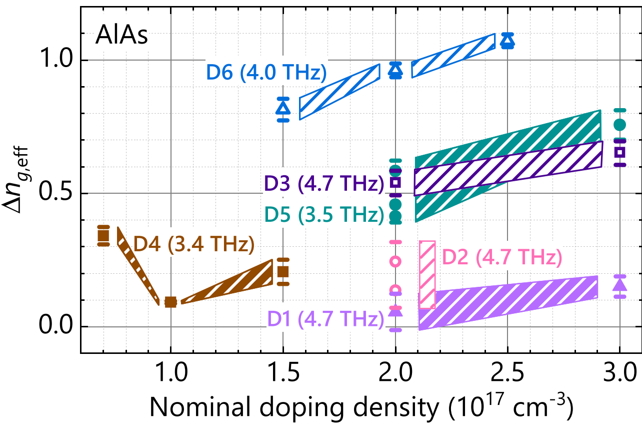

Figure 6. Deviation $\Delta n_{g,\text{eff}} = n_{g,\text{eff}} - \bar{n}_{g,\text{eff}}$ from the general trend of different QCLs with AlAs barriers as a function of the nominal doping density. Same symbols indicate the results for identical designs of the layer sequence. The different layer sequences are referred to as D1 to D6. For clarity, the error ranges are merged so that only the top- and bottommost error bars for every group of symbols (same nominal doping density and design of the layer sequence) are shown. The hatched areas connect the data points of the same designs and serve as a guide to the eye. For the nominal doping density of 2×10^{17} cm^{-3}, there are two data points for D2 and three data points for D5, which represent results from different wafers (regrowth).

these differences in $\Delta n_{g,\text{eff}}$ depending on the particular design modification may be due to differences in the gain/loss spectra. Due to the high complexity of the hybrid design scheme and hence of the subband structure and carrier transport, tracking the influence of the design modifications on $n_{g,\text{eff}}$ quantitatively is very challenging, even with the help of simulations, which are described in the following subsection 3.3. Instead, we interpret the results shown in figure 6 more qualitatively as evidence for an influence of the design modification on $n_{g,\text{eff}}$.

Figure 6 also shows a small dependence of $\Delta n_{g,\text{eff}}$ on the nominal doping density. This dependence may be mediated by the dielectric response of the free carriers. The relevant measure of the number of free carriers is the nominal doping density of a single period of the active region, which is given by the nominal doping density multiplied by the ratio of the thickness of the doped layer and the thickness of one period of the active region (every period contains one doped layer). The values for the nominal doping density of the doped layer as shown in figure 6 correspond to a nominal doping density of a single period between 0.7 and 4.4×10^{16} cm^{-3}. Considering $\Delta n_{g,\text{eff}}$ as a function of the nominal doping density of a single period yields a qualitatively similar result as in figure 6, since the thicknesses of the injector layers do not scale with the emission frequency. In particular, $\Delta n_{g,\text{eff}}$ mostly increases with the nominal doping density of a single period, while the opposite trend is expected from a Drude model for free-carrier absorption [41]. This result suggests that the dielectric response of the free carriers is negligible so that the nominal doping density influences $n_{g,\text{eff}}$ mainly through its effect on the subband structure. In order to validate the results shown in figure 6, we have verified that the investigated QCL stripes are located at similar positions on the wafer (at a distance of about 10 mm from the edge).

The growth of THz QCLs is very challenging due to the very thin barriers and the very large total thickness of the active region. Consequently, small variations in the growth conditions may have a significant influence on the characteristics of THz QCLs. In order to investigate variations in $n_{g,\text{eff}}$ due to changes in the growth conditions over time, figure 7 shows $\Delta n_{g,\text{eff}}$ as a function of a sequential wafer number. Wafers with a larger sequential number were grown later. The wafers of the same design of the layer sequence (regrowth or modified nominal doping density) were grown at a similar point in time (difference in sequential number smaller than 100).

Figure 7 shows a tendency toward larger values of $\Delta n_{g,\text{eff}}$ with increasing sequential wafer number. This result indicates a variation of the growth conditions over time, which may affect the structural quality such as the interface roughness of the wafers and hence $\Delta n_{g,\text{eff}}$ of the corresponding QCLs. A possible mechanism for these results will be discussed in subsection 3.3. Figure 7 also shows the influence of the design of the layer sequence on $\Delta n_{g,\text{eff}}$. For example, QCLs of design D3 exhibit significantly larger values for $\Delta n_{g,\text{eff}}$ than QCLs

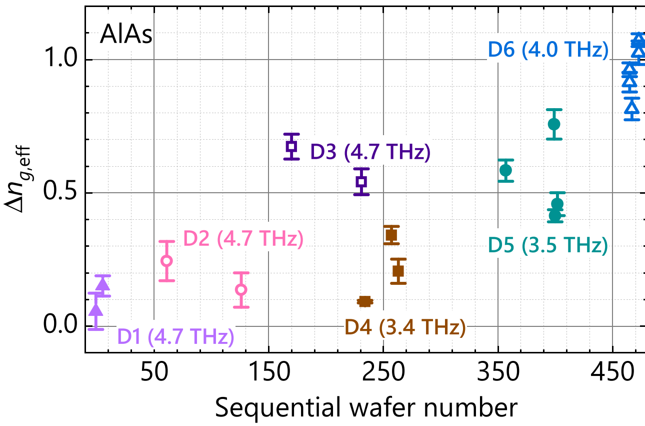

Figure 7. Deviation $\Delta n_{g,\mathrm{eff}} = n_{g,\mathrm{eff}} - \bar{n}_{g,\mathrm{eff}}$ from the general trend as a function of a sequential wafer number for QCLs with AlAs barriers. The symbols group wafers of the same design, which may vary in the nominal doping density.

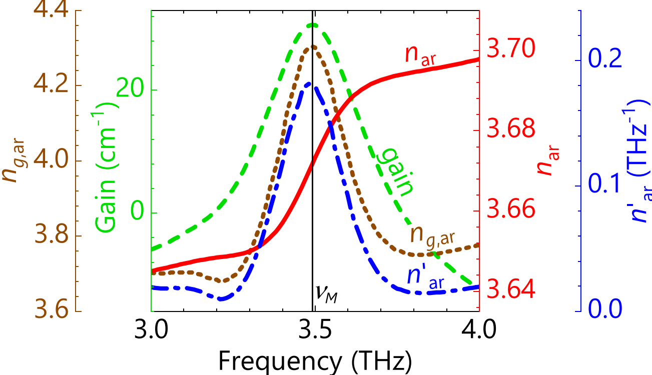

Figure 8. Prototypical example of the simulation results for the gain, the phase refractive index n_{ar}, its derivative n'_{ar}, and the group refractive index $n_{g,\mathrm{ar}}$ of an active region for 3.5 THz. The vertical line indicates the frequency ν_M of the gain maximum. The simulation results for the refractive indices take into account the presence of intersubband transitions and a background dielectric refractive index of 3.61. The selected electric field strength amounts to 0.1 kV/cm above threshold.

of design D4, although they were grown at similar points in time.

Apart from the design and the growth conditions, we also investigated whether there is a relationship between $\Delta n_{g,\mathrm{eff}}$ and the performance characteristics such as the maximum output power based mainly on the QCLs shown in figure 7. We could not find any dependence of $\Delta n_{g,\mathrm{eff}}$ on the threshold current density, the maximum output power, the dynamic range of the injection current, or the emission bandwidth (not shown).

3.3. Intersubband transitions

Intersubband transitions have recently been found to substantially contribute to the dynamic tuning of THz QCLs by means of the injection current [35]. These transitions affect the refractive index through optical gain or loss, which can be explained with the Lorentz oscillator model. Consequently, the presence of intersubband transitions is also expected to affect $n_{g,\mathrm{eff}}$. From the simulations of active regions with our Fourier transform-based model [42, 43], we obtain both, the gain/loss spectra and the frequency-dependent material refractive index n_{ar} of the active region (ar). Figure 8 shows an example of the simulation results based on a field strength at the onset of gain clamping for a THz QCL emitting at about 3.5 THz. The value of the refractive index n_{ar} increases from about 3.645 to about 3.7 over the displayed frequency range. At the position of the inflection point of n_{ar}, which is located at the frequency ν_M of the gain maximum, the derivative

$$n'_{\mathrm{ar}} = \frac{\partial n_{\mathrm{ar}}}{\partial \nu} \tag{5}$$

exhibits its maximum. Thus, a qualitatively similar curve is obtained for the group refractive index $n_{g,\mathrm{ar}}$, since it is given by [28]:

$$n_{g,\mathrm{ar}} = n_{\mathrm{ar}} + \nu n'_{\mathrm{ar}} \, . \tag{6}$$

Quantitatively, the value for $n_{g,\mathrm{ar}}$ is increased to 4.3 at ν_M with respect to the values of 3.7 and 3.8 at the edges of the displayed frequency range, which clearly shows that the presence of optical gain resulting from intersubband transitions leads to a significant enhancement of $n_{g,\mathrm{ar}}$ close to ν_M. Note that $n_{g,\mathrm{ar}}$ at ν_M can even be affected by the gain/loss at frequencies substantially different from ν_M, which is illustrated by a refractive index larger than the background index of 3.61 for the entire frequency range shown in figure 8. In the investigated structure, this higher value originates from a strong absorption line at about 5.5 THz (not shown).

The simulations as described above can be employed to investigate whether different active-region designs also exhibit different values of $n_{g,\mathrm{ar}}$ at the respective gain maxima. Such differences are expected from the experimental results displayed in figure 6. Indeed, our simulations show a considerable variation of $n_{g,\mathrm{ar}}$ depending on the particular design. However, these simulation results do not quantitatively agree with the experimental results displayed in figure 6, although we also took into account waveguide dispersion using electromagnetic simulations. We attribute the rather limited predictability of our model to the comparatively complex subband structure of our active-region designs [27]. Since our model is based on approximations for the carrier transport, the simulation results for complex structures are expected to be of limited quantitative accuracy. Similarly, a reduced predictability for complex structures has been observed in the analysis of the current-induced tuning based on the same model [35].

Another important parameter affecting the optical properties of the QCLs is the inhomogeneous broadening of the gain spectra, which is attributed to interface roughness including alloy disorder and lateral fluctuations of the doping density. Figure 9 shows simulation results for similar quantities as in figure 8 as a function of the broadening factor Γ_0 described in [35, 44]. An increased broadening leads to a wider gain spectrum (in terms of the full width at half maximum, FWHM) and

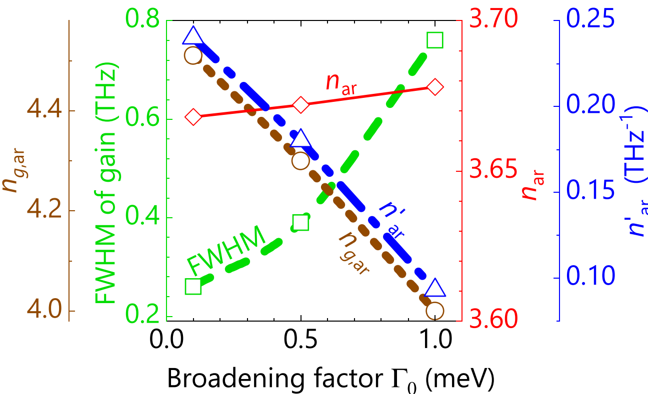

Figure 9. Simulation results of the full width at half maximum (FWHM) of the gain curve (rectangles), the group refractive index $n_{g,\mathrm{ar}}$ at the frequency ν_M of the gain maximum (circles), the phase refractive index n_{ar} at ν_M (diamonds), and the derivative n'_{ar} at ν_M (triangles) for the active region (ar) as a function of the broadening factor Γ_0.

reduced slope n'_{ar}, resulting in lower values for $n_{g,\mathrm{ar}}$ according to equation (6) as n_{ar} remains rather constant. We conclude that a large value of $n_{g,\mathrm{ar}}$ may indicate a low level of interface roughness. As electromagnetic simulations show, $n_{g,\mathrm{eff}}$ follows the trend of $n_{g,\mathrm{ar}}$, linking the interface roughness to the experimentally accessible values of $n_{g,\mathrm{eff}}$. This result agrees with the experimental evidence for a relationship between $n_{g,\mathrm{eff}}$ and the structural quality as shown in figure 7. A difficulty to apply this relationship in practice may be the additional dependence of $n_{g,\mathrm{eff}}$ on design details and on the actual layer sequence of the grown structure. Note that a large width of the gain profile does not imply a large emission bandwidth, since the emission bandwidth also depends on the height of the (small-signal) gain curve.

An experimental verification of the correspondence between a larger value for $n_{g,\mathrm{eff}}$ and a reduced interface roughness will be subject to further experimental studies including examinations of QCL structures by transmission electron microscopy.

4. Conclusions

We have investigated the effective group refractive index $n_{g,\mathrm{eff}}$ for a large number of THz QCLs based on the hybrid design by analyzing their emission spectra. The values for $n_{g,\mathrm{eff}}$ as a function of emission frequency follow a general trend for most of the GaAs/Al$_x$Ga$_{1-x}$As and GaAs/AlAs QCLs, which is mainly determined by material and waveguide dispersion. However, a considerable number of GaAs/AlAs QCLs exhibit substantial deviations from this trend. We ruled out a significant correlation between this deviation and different structural parameters, i.e. the average Al content, the thickness of the active regions, the nominal doping density, and the position of the investigated QCL stripes on the wafer. We also excluded a significant correlation with the performance characteristics such as the output power. In contrast, our simulations provide evidence for the dependence of $n_{g,\mathrm{eff}}$ on the gain/loss spectra resulting from intersubband transitions in the active region, which can explain the experimentally observed variation in $n_{g,\mathrm{eff}}$ depending on the layer sequence of the active region. Furthermore, the simulations show that $n_{g,\mathrm{eff}}$ depends substantially on the inhomogeneous broadening of the gain spectra. The broadening is mainly attributed to interface roughness including alloy disorder and a laterally inhomogeneous doping density. Hence, $n_{g,\mathrm{eff}}$ is related to the structural quality of the QCLs, which is in agreement with an observed correlation between $n_{g,\mathrm{eff}}$ and the date of growth of the wafers. GaAs/AlAs QCLs may be particularly sensitive to the growth conditions due to their very thin barriers. If the influence of the interface roughness on $n_{g,\mathrm{eff}}$ is confirmed by further experimental techniques such as transmission electron microscopy, the determination of $n_{g,\mathrm{eff}}$ may provide a straightforward path to assess the structural quality of THz QCLs.

Acknowledgments

We would like to thank M Wienold and R Sharma for the experimental data of many GaAs/(Al,Ga)As QCLs as well as W Anders, R Hey, M Höricke, A Riedel, and A Tahraoui for the preparation of the samples. We are grateful to A Crespo-Poveda and S Kurlov for a critical reading of the manuscript as well as to E Luna for fruitful discussions. Partial financial support of this work by the Leibniz-Gemeinschaft under Grant No. K54/2017 is gratefully acknowledged.

ORCID iDs

Benjamin Röben https://orcid.org/0000-0003-4356-5741
Xiang Lü https://orcid.org/0000-0001-7169-7771
Klaus Biermann https://orcid.org/0000-0003-4804-0784
Lutz Schrottke https://orcid.org/0000-0002-0910-9163
Holger T Grahn https://orcid.org/0000-0001-5451-3950

References

[1] Köhler R, Tredicucci A, Beltram F, Beere H E, Linfield E H, Davies A G, Ritchie D A, Iotti R C and Rossi F 2002 *Nature* **417** 156
[2] Ulrich J, Zobl R, Finger N, Unterrainer K, Strasser G and Gornik E 1999 *Physica* B **272** 216
[3] Williams B S, Kumar S, Callebaut H, Hu Q and Reno J L 2003 *Appl. Phys. Lett.* **83** 2124
[4] Burghoff D *et al* 2014 *Nat. Photon.* **8** 462
[5] Wienold M, Röben B, Schrottke L and Grahn H T 2014 *Opt. Express* **22** 30410
[6] Yang Y, Burghoff D, Hayton D J, Gao J R, Reno J L and Hu Q 2016 *Optica* **3** 499
[7] Rösch M, Scalari G, Villares G, Bosco L, Beck M and Faist J 2016 *Appl. Phys. Lett.* **108** 171104
[8] Wienold M, Röben B, Schrottke L, Sharma R, Tahraoui A, Biermann K and Grahn H T 2014 *Opt. Express* **22** 3334
[9] Bosco L, Franckie M, Scalari G, Beck M, Wacker A and Faist J 2019 *Appl. Phys. Lett.* **115** 010601
[10] Richter H *et al* 2010 *Opt. Express* **18** 10177
[11] Schrottke L *et al* 2020 *IEEE Trans. Terahertz Sci. Technol.* **10** 133

[12] Hagelschuer T, Richter H, Wienold M, Lü X, Röben B, Schrottke L, Biermann K, Grahn H T and Hübers H-W 2019 *IEEE Trans. Terahertz Sci. Technol.* **9** 606
[13] Rösch M, Scalari G, Beck M and Faist J 2015 *Nat. Photon.* **9** 42
[14] Burghoff D, Yang Y, Reno J L and Hu Q 2016 *Optica* **3** 1362
[15] Bachmann D, Rösch M, Scalari G, Beck M, Faist J, Unterrainer K and Darmo J 2016 *Appl. Phys. Lett.* **109** 221107
[16] Röben B, Wienold M, Schrottke L and Grahn H T 2016 *AIP Adv.* **6** 065104
[17] Eichholz R, Richter H, Pavlov S G, Wienold M, Schrottke L, Hey R, Grahn H T and Hübers H-W 2011 *Appl. Phys. Lett.* **99** 141112
[18] Dean P *et al* 2012 *Semicond. Sci. Technol.* **27** 094004
[19] Röben B, Lü X, Hempel M, Biermann K, Schrottke L and Grahn H T 2017 *Opt. Express* **25** 16282
[20] Wienold M, Alam T, Schrottke L, Grahn H T and Hübers H-W 2018 *Opt. Express* **26** 6692
[21] Hübers H-W, Richter H and Wienold M 2019 *J. Appl. Phys.* **125** 151401
[22] Hofstetter D and Faist J 1999 *IEEE Photon. Technol. Lett.* **11** 1372
[23] Gmachl C, Soibel A, Colombelli R, Sivco D L, Capasso F and Cho A Y 2002 *IEEE Photon. Tech. Lett.* **14** 1671
[24] Kester M and Ippen E 1989 *Electron. Lett.* **25** 640
[25] Choi H Y, Diehl L, Capasso F, Bour D, Corzine S, Zhu J T, Höfler G and Norris T B 2007 *Opt. Express* **15** 15898
[26] Yang Q, Kinzer M, Aidam R, Driad R, Bronner W, Hugger S, Ostendorf R, Fuchs F and Wagner J 2012 *J. Appl. Phys.* **112** 103109
[27] Schrottke L, Lü X, Rozas G, Biermann K and Grahn H T 2016 *Appl. Phys. Lett.* **108** 102102
[28] Röben B, Lü X, Biermann K, Schrottke L and Grahn H T 2019 *J. Appl. Phys.* **125** 151613
[29] Wienold M, Schrottke L, Giehler M, Hey R, Anders W and Grahn H T 2009 *Electron. Lett.* **45** 1030
[30] Köhler R, Tredicucci A, Mauro C, Beltram F, Beere H E, Linfield E H, Davies A G and Ritchie D A 2004 *Appl. Phys. Lett.* **84** 1266
[31] Scalari G, Hoyler N, Giovannini M and Faist J 2005 *Appl. Phys. Lett.* **86** 181101
[32] Moore W J and Holm R T 1996 *J. Appl. Phys.* **80** 6939
[33] Wienold M, Tahraoui A, Schrottke L, Sharma R, Lü X, Biermann K, Hey R and Grahn H T 2012 *Opt. Express* **20** 11207
[34] Saleh B E A and Teich M C 2007 *Fundamentals of Photonics* 2nd edn (New York: Wiley)
[35] Schrottke L, Lü X, Röben B, Biermann K, Wienold M, Richter H, Hübers H-W and Grahn H T 2018 *J. Appl. Phys.* **123** 213102
[36] Wienold M, Röben B, Schrottke L, Sharma R, Tahraoui A, Biermann K and Grahn H T 2014 *Opt. Express* **22** 3334
[37] Wienold M, Schrottke L, Giehler M, Hey R, Anders W and Grahn H T 2010 *Appl. Phys. Lett.* **97** 071113
[38] Schrottke L *et al* 2013 *Semicond. Sci. Technol.* **28** 035011
[39] Amanti M I, Scalari G, Terazzi R, Fischer M, Beck M, Faist J, Rudra A, Gallo P and Kapon E 2009 *New J. Phys.* **11** 125022
[40] Lü X, Luna E, Schrottke L, Biermann K and Grahn H T 2018 *Appl. Phys. Lett.* **113** 172101
[41] Harrison P and Valavanis A 2016 *Quantum Wells, Wires and Dots: Theoretical and Computational Physics of Semiconductor Nanostructures* 4th edn (New York: Wiley)
[42] Schrottke L, Lü X and Grahn H T 2015 *J. Appl. Phys.* **117** 154309
[43] Lü X, Schrottke L and Grahn H T 2016 *J. Appl. Phys.* **119** 214302
[44] Schrottke L, Wienold M, Giehler M, Hey R and Grahn H T 2010 *J. Appl. Phys.* **108** 103108